Localized Orbital Excitation Drives Bond Formation in Plasmonic Catalysis

Mou, Tong

2021-12-07

Mou , T , Quiroz , J , Camargo , P H C & Wang , B 2021 , ' Localized Orbital Excitation Drives Bond Formation in Plasmonic Catalysis ' , ACS Applied Materials & Interfaces , vol. þÿ1 3 , n o . 5 0 , p p . 6 0 1 1 5 6 0 1 2 4 . h t t p s : / / d o i . o r g / 1 0 . 1 0 2 1 / a c s a m i . 1 c 2 1 6 0

http://hdl.handle.net/10138/353719
https://doi.org/10.1021/acsami.1c21607

unspecified
acceptedVersion

Localized Orbital Excitation Drives Bond Formation in Plasmonic Catalysis

*Tong Mou[1,2], Jhon Quiroz[3], Pedro H. C. Camargo[3] and Bin Wang[1,]**

[1]*Center for Interfacial Reaction Engineering and School of Chemical, Biological and Materials Engineering, Gallogly College of Engineering, University of Oklahoma, Norman, Oklahoma 73019, United States*

[2]*Shenzhen JL Computational Science and Applied Research Institute, Shenzhen, Guangdong 518131, China*

[3]*Department of Chemistry, University of Helsinki, 00560 Helsinki, Finland*

**Corresponding author: wang_cbme@ou.edu*

ABSTRACT: Localized surface plasmons generated on metallic nanostructures can be used to accelerate molecular transformations; however, the efficiency is limited by the challenge to control the energy/charge transfer at the interfaces. Here, we combine density functional theory (DFT) calculations and experiments to reveal the mechanism of nitrophenol reduction on Au nanoparticles under visible-light irradiation and propose a strategy to further enhance the reaction rates. DFT calculations show a reduced activation barrier under electronic excitation on Au(111), thus explaining the measured higher rates under visible-light irradiation. Furthermore, we propose a heterostructure with Au nanoparticles covered by a thin film of hexagonal boron nitride; the latter is used to decouple the molecular orbitals from the metal to enable charge localization in the molecule. DFT calculations show that, by this electronic decoupling, the activation barrier can be lowered by a factor of five. This work thus provides a valuable strategy for optimizing catalytic efficiency.

Keywords: Hot electrons, bond formation, DFT, nitroarene hydrogenation, LSPR

1. Introduction

Conventionally, thermal energy is supplied to accelerate a rate-limiting step in a chemical reaction; however, increasing reaction temperature triggers every available reaction coordinate in the system and therefore enhances simultaneously desired and competing undesired elementary steps, reducing selectivity to the desired products. In addition, high operating temperature greatly affects thermal stability of catalysts and reduces catalyst lifetime. Plasmonic catalysis, on the other hand, opens an avenue to a low-temperature, highly selective and environmentally benign process to accelerate and control chemical transformations.[1–4] Because of this unique potential, plasmonic

catalysis has received extensive attention in recent years,[5–8] and the concept has been applied in many reactions such as N_2 dissociation,[3,9] H_2 dissociation,[10,11] NH_3 decomposition,[12,13] nitrite reduction[14,15] and hydrogenation of unsaturated aromatic bonds.[16]

In plasmonic catalysis, metal nanoparticles such as Ag, Au, Cu, and Al can serve as light absorbers without the involvement of semiconductor materials. In these metal nanoparticles (NPs) upon visible-light absorption, surface plasmons are produced from the couplings between the metal valence electrons and the incident photons through the excitation of localized surface plasmon resonances (LSPRs), as long as the size of the metal nanoparticles is equal or smaller than the light wavelength.[5,6] The small imaginary dielectric function of these noble metals (Ag, Au, Cu) leads to a large optical extinction cross-section of a plasmonic nanoparticle at LSPR frequencies.[17,18]

Excitation of the LSPRs has been proposed to drive the chemical reactions of neighboring molecules through energy and charge transfer.[10,19] A few mechanisms have been discussed in the literature related to the nature of energy and charge transfer across the interface between plasmonic materials and their local environment as shown in Scheme 1.[5,6] For example, harvesting and transferring the plasmonic excitation energy to the adsorbed molecules through plasmonic-induced resonance energy transfer (PIRET) has been discussed extensively in plasmonic catalysis.[3,9,20,21] In addition, charge transfer, both directly and indirectly, have been proposed for some other plasmonic reactions.[10,19,22,23] In the indirect charge transfer mechanism (Landau damping, LD), excited surface plasmons decay non-radiatively upon photon absorption to form highly energetic electrons and holes,[24,25] and these so-called "hot" carriers, while having enough kinetic energy, can be transferred to the adjacent substrate molecules[10,26,27] or semiconductors.[28,29] This indirect mechanism in principle does not allow selective charge transfer to specific molecular orbitals in the adsorbate. Different from this indirect charge transfer process that is mediated by hot electrons, direct charge excitation to the interfacial electronic states through chemical interface damping (CID) is possible within the metal-adsorbate complex such as in methylene blue on Ag NPs.[5,22,23] This direct charge transfer can also be manipulated to target occupation of specific molecular orbitals towards desired selectivity by breaking or forming a chemical bond.[30,31] Indeed, many previous works have shown that electron-induced plasmonic catalysis can influence reaction selectivity.[16,32]

Despite the significant progress in light-induced rate enhancements, the efficiency of plasmon-mediated photocatalytic process is still much lower than that on traditional

semiconductor-based photocatalysts. There are a few factors that might be responsible for the low efficiency: highly energetic carriers have short lifetime due to fast recombination rate in femtosecond range;[33] charge carriers with energy lower than required energy to populate the accessible antibonding states are wasted in the form of phonons (heat). Furthermore, previous experimental or theoretical studies mostly focused on bond dissociation events;[2,10,19] there have been few studies[13,20] investigating if these energy and/or charge transfer can also assist bond formation (Scheme 1). In many practical industrial chemical processes, such as hydrotreating in refineries and ammonia synthesis, bond association is a key elementary step. Finally, orbital hybridization between the plasmonic metal and the adsorbate frontier orbitals significantly broaden the latter, making it very challenging for selective energy and charge transfer to targeted orbitals for specific bond formation and breaking, which limits the overall photon-to-chemical conversion efficiency and reaction selectivity.

Here, we present combined experimental and theoretical results of 4-nitrophenol (4-NPh) hydrogenation on gold nanoparticles, through which we show that electronic excitation can stimulate the reaction, and that this effect can be further enhanced if the excited electrons can be localized at the molecular orbital that is electronically decoupled from the plasmonic metal. Specifically, we measured the catalytic activity on Au catalysts with and without light irradiation and observed higher reaction rates under the light. The effect of light was then elucidated by the comparison of the ground-state (without electronic excitation) and excited-state (with electronic excitation) potential energy surfaces (PES) based on standard density functional theory (DFT) and delta self-consistent field (ΔSCF) calculations, as previously done by us.[34] We observed a reduced activation barrier with electronic excitation. However, due to the degeneracy of molecular orbitals and the metal extended s orbitals, it is challenging to ambiguously identify the role of the excited electrons in lowering the activation barrier. We thus propose to decouple the molecular frontier orbitals from Au by inserting a thin layer of hexagonal boron nitride (*h*-BN). Our analysis shows the activation barrier of the rate-limiting step for reduction of 4-nitrophenol is significantly lowered because of localized charge in the molecular frontier orbital.

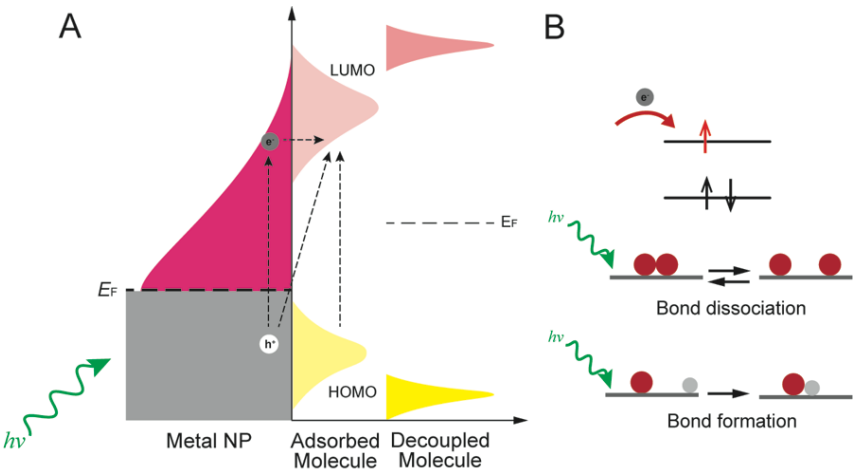

Scheme 1. Mechanisms of plasmon-driven photocatalysis on metal NPs under light irradiation. A. Schematic diagram of electronic excitation and energy/charge transfer under visible light. Hybridization between the metal s states and the molecular frontier orbitals results in accessible molecular orbitals in the range of visible light. B. Bond dissociation could be assisted by adding an electron into the anti-bonding orbital of the molecule. The role of energy/charge transfer in plasmonic bond formation could be distinct from the bond dissociation mechanism.

2. Methods

2.1 Computational details

All density functional theory calculations were carried out using Vienna Ab initio simulation package (VASP)[35], version vasp.5.4.1. The Perdew-Burke-Ernzerhof generalized gradient approximation exchange-correlation potential (PBE-GGA)[36] was used, and the valence electron wave function were treated in the projector augmented wave (PAW)[37,38] method with a kinetic cutoff energy of 400 eV. The van der Waals interaction has been taken into account through Grimme's DFT-D3 semiempirical method.[39] The reactions were modeled accordingly. Gaussian smearing (width = 0.2 eV) was used to calculate the partial occupancies. The structures were relaxed until the force acts on each atom is smaller than 0.02 eV $Å^{-1}$. The electronic energy convergence was set to 1.0×10^{-5} eV / atom.

Au(111) was chosen to represent the energetically most stable facet. The close-packed Au(111) slab was modeled with a 4 × 4 supercell composed of four atomic layers and 20 Å of vacuum between the slabs in the Z-direction. The bottom two layers were frozen to emulate the bulk, while the top two layers and molecules positioned above the Au surface were allowed to

relax. The Brillouin zone was sampled with a 3 × 3 × 1 k−point grid for structural optimizations, and a 6 × 6 × 2 k−point grid for the density of states (DOS) calculations under this study.

To model the monolayer hexagonal boron nitride (*h*-BN), a boron nitride unit cell was optimized and cleaved in the (0 0 1) direction to form a graphenelike honeycomb structure consisting of 16 B and 16 N atoms. The BN layer was placed in the middle of the box and a large spacing of 15 Å was added to avoid interactions between layers. To model the carbon-doped *h*-BN monolayer, an N atom was replaced by a C atom, resulting in the C-B bond length being 1.49 Å, which is 0.05 Å longer than the B-N bond length (1.44 Å) in the pristine *h*-BN monolayer.

Transition state searches were performed using the dimer method[40] with the initial guesses for the transition state structure obtained through the nudged elastic band (NEB) method with eight images between initial and final states.[41] The transition states were confirmed with the presence of a unique imaginary frequency in the vibration frequency calculations. The minimum-energy paths for the reactions were then determined.

The Bader charge analysis was implemented to determine the charge state localized on each atom in the system.[42]

The adsorption energy (E_{ads}) was calculated as $E_{ads} = E_{i/slab} - (E_{slab} + E_i)$ where $E_{i/slab}$, E_{slab}, E_i are the energies of the slabs with the adsorbed molecule, the clean metal slab, and the molecule in the gas phase, respectively. The energies of the adsorbates and gas phase molecules were calculated using a 10×10×10 supercell with a gamma-only k-point mesh.

To map the excited-state energy curves, an additional electron was added to different Kohn-Sham (KS) orbitals to simulate hot electron excitation from Au, while the hole was assumed to stay within Au. In order to estimate the excitation energy for electrons traveling from Au to 4-NPh molecule, the partial density of states and band separation calculations were performed. With the estimated excitation energy, by using delta self-consistent field extension of DFT (ΔSCF-DFT),[43] the excited-state energy curves along the minimum-energy path of the rate-limiting step was calculated. In this method, we first calculated and interpreted KS orbitals as the molecular orbital, and the relevant KS orbitals were analyzed and identified through analysis of the local density of states and the electron density of each KS orbital. Then, the occupation in the relevant KS orbitals was modified and the system was relaxed self-consistently in a way that keeps the electron/hole in the relevant KS orbitals to model excited states.[44]

The reaction coordinates in reaction profiles are defined by the equation below:

$$\mathrm{RC}(m, m+1)(\text{Å}) = \|\mathbf{RC}\| = \sum_{i=1}^{N}(\boldsymbol{x_{m+1,i}} - \boldsymbol{x_{m,i}}, \boldsymbol{y_{m+1,i}} - \boldsymbol{y_{m,i}}, \boldsymbol{z_{m+1,i}} - \boldsymbol{z_{m,i}}) \quad (1)$$

Where m is the initial structure at ground-state, m+1 is the corresponding state as referenced to the x, y, z value in the ground-state initial structure, and i represents each atom in the system.

2.2 Synthesis of Au NPs.

Au NPs were prepared by the citrate reduction approach.[45] In a typical procedure, 95 mL of H_2O were mixed with 5 mL of 0.5 wt. % sodium citrate trihydrate in a 250 mL round-bottom flask. This system was heated to 100 °C for 15 minutes under magnetic stirring followed by the addition of 2 mL of an aqueous solution of $AuCl_4^-$ 25mM. The reaction proceeded for approximately 10 minutes yielding a red suspension containing the Au nanoparticles.

2.3 4-Nitrophenol hydrogenation by $NaBH_4$ catalyzed by Au NPs.

All the hydrogenation reactions were performed in a quartz cuvette and monitored using a UV/VIS spectrophotometer ranging from 250 nm to 500 nm. In a typical procedure, 1.5 mL of a 0.14 mM 4-nitrophenol aqueous solution was mixed in a quartz cuvette with 0.25 mL of freshly prepared 42 mM sodium borohydride solution. Afterwards, 100 L of 0.5 mM aqueous suspension containing the Au NPs were added to the quartz cuvette and this instant was defined as the reaction starting time (t = 0). To calculate the conversion of 4-nitrophenol, the change in absorption of the band at 400 nm was monitored. In order to obtain different 4-NPh/BH_4^- molar ratios, we varied the volume of the 42 mM sodium borohydride solution added to the reaction, corresponding to 5, 25, 50, 250 and 500 L for 1:1, 1:5, 1:10, 1:50 and 1:100 molar ratios, respectively. For reactions carried out under visible light excitations, a LED green lamp (525 nm) was employed as the excitation source. The lamp was set 10 cm away from the reactor, and the position and distance of the lamp onto the reaction were kept constant in all experiments. The potency impinging the reactor corresponded to 10 mW/cm^2.

3. Results and discussion

3.1 Reduction of 4-NPh on Au surfaces.

Prior work showed that the catalytic reduction of 4-NPh on Au and Ag nanoparticles could be enhanced under resonant illumination (532 nm);[14,45] however, the mechanism has not yet been

reported. We have measured herein the conversion as a function of time for the 4-NPh hydrogenation by BH_4^-(aq) on Au NPs under LSPR excitation by a green LED light source, with various 4-NPh:BH_4^- molar ratios. We use BH_4^-(aq) as the reduction agent to avoid the slow dissociation kinetics of H_2 on the Au surface.[45] External heating was not employed. The conversion under LSPR excitation is strongly dependent on the 4-NPh:BH_4^- molar ratios, increasing with the proportion of BH_4^-. The initial rate constants, calculated up to 5s of reaction, are shown in Table 1. The conversion and initial rate constants under light excitation are higher than ones under similar conditions without light irradiation for all 4-NPh:BH_4^- molar ratios (Figure S1). This result is in agreement with our previous reports,[45] which showed that the reaction rates for this chemical transformation on SiO_2-supported Au was enhanced by LSPR excitation.

This enhancement is unlikely caused by thermal heating because of a distinct trend observed over TiO_2-supported Au under LSPR excitation in our previous report.[45] That is, decrease in reaction rate was observed under LSPR excitation over TiO_2-supported Au using the same reduction agent; this decrease of rate was attributed to charge transfer into TiO_2 by the built-in electric field at the interface.[45] This distinct behavior between SiO_2- and TiO_2-supported Au under the same reaction conditions indicates that plasmonic heating is not the driving force, which otherwise should enhance rates in both systems. Instead, charge transfer through LSPR excitation is likely the predominant factor for the enhanced rates over SiO_2-supported Au.

Table 1. The initial rate constants calculated at various 4-NPh:BH_4^- molar ratios under dark and LSPR excitation.

4-NPh/BH_4^- molar ratios	Initial rate constant k (10^5 mol·L^{-1}·min^{-1})	
	Dark	LSPR excitation
1:1	0.0258	0.0264
1:5	2.3281	3.8724
1:10	7.2598	8.6896
1:50	10.9878	11.9845
1:100	16.2246	19.1212

3.2 DFT Calculations of the reaction profile at the ground state.

In the following we explore the reaction mechanism by performing DFT calculations. We first compared different adsorption configurations of 4-nitrophenol on an Au(111) surface (the most stable facet) to determine the most stable structure (Figure S2) without any additional charge. It turns out that the adsorption of 4-NPh preferentially takes place on the fcc site entailing the molecule lying flat on the surface. The aromatic ring interacts with four Au atoms to maximize the d-π interaction (Figure 1A). Oxygen atoms from the nitro group bind closer to the surface than the aromatic ring due to their high electrophilicity (Figure 1B). This configuration is similar to previously reported adsorption modes of nitroarene on nickel, platinum and other metals.[46,47] The adsorption energy of 4-NPh is -102 kJ/mol with the van der Waals corrections. Accordingly, the distances between O_1 and O_2 (labelled in Figure 1B) in the nitro group and the nearest Au atom are 3.23 and 3.03 Å, respectively. On the other hand, the interaction of borohydride ions with Au NPs produces adsorbed H species,[48,49]

$$BH_4^- + H_2O + 2^* \rightarrow BH_3(OH)^- + 2H^* \quad (2)$$

The overall reduction proceeds as shown in the equation below (Eq. 2):

$$R - NO_2 + 3NaBH_4 + 3H_2O \rightarrow R - NH_2 + 3NaBH_3(OH) + 2H_2O \quad (3)$$

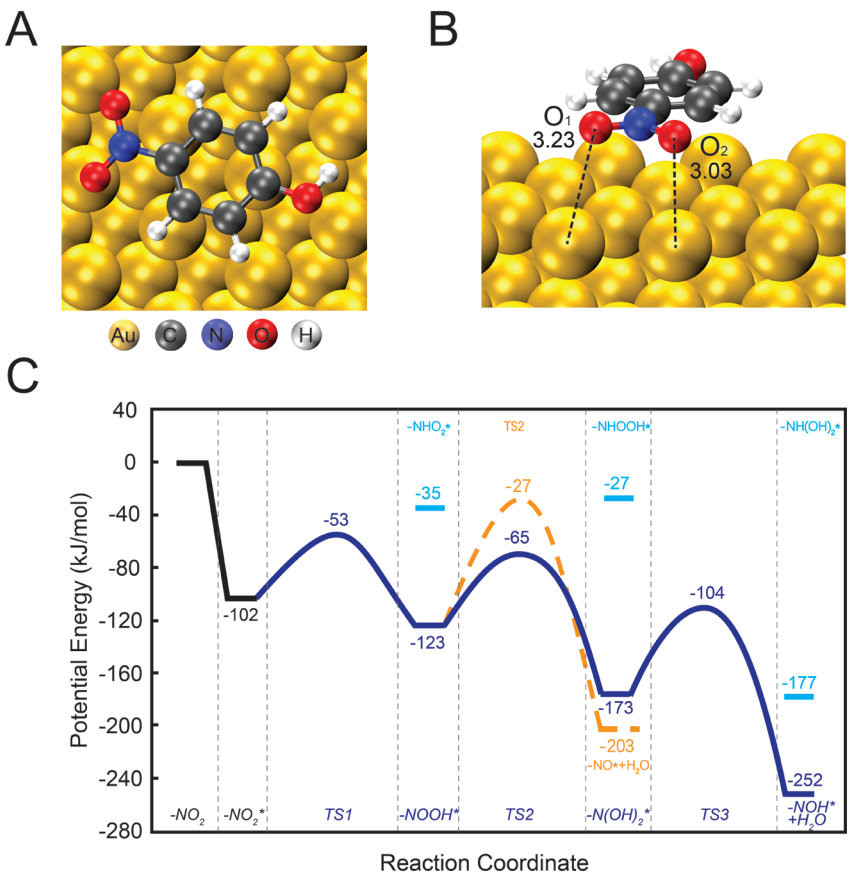

Figure 1. Optimized geometries of 4-nitrophenol on Au(111): Top view (A) and side view (B) of the most stable adsorption structure. C. The potential energy profile for the 4-nitrophenol hydrogenation (first three hydrogenation steps) catalyzed by Au. The most favorable reaction path is connected with black lines, while the reaction paths following alternate hydrogenation sequences are shown in blue and yellow.

We then computed the kinetic barriers of 4-NPh reduction to 4-aminophenol (4-APh) on Au(111) to identify the rate-determining step (RDS). Here we analyzed the reaction kinetics of surface-adsorbed species in terms of the Langmuir-Hinshelwood mechanism,[50] in which both reactants (4-NPh and H) adsorb on the catalyst surface to react. Previous study showed that formation of surface-hydrogen species via borohydride ions on the Au surface is reversible and fast, which can be modeled by the Langmuir-Freundlich isotherm.[49] Also, the adsorption of 4-NPh and desorption of products are fast, so that the RDS takes place between surface-hydrogen and adsorbed species.[50] The reduction reaction of 4-NPh to the corresponding 4-APh on metal catalysts is a six-electron transfer process.[51] It is important to note that adding the first hydrogen on O_1 (labelled in Figure 1B) exhibits similar energy barrier to adding it on O_2, so that only one case is

shown here. Figure 1C summarizes the most likely potential energy profile from ground-state calculations. All the energies reported here do not consider lateral interactions between adsorbates. The first hydrogenation on O_2 in the nitro moiety to form R-NO(OH)* has a true activation barrier of 49 kJ/mol and reaction energy of -21 kJ/mol. The hydrogenation of N as the first step is highly unfavorable thermodynamically with an energy cost of 67 kJ/mol. After hydrogenating the O_2 atom in the nitro moiety, the second hydrogenation has several possible pathways. The energy cost for hydrogenation of N is still high, 96 kJ/mol. Alternatively, we examined hydrogen attack to the hydroxyl group forming a water molecule, which is highly exothermic (-80 kJ/mol), due to the formation of two stable intermediates (R-NO* and H_2O), but renders a high activation barrier of 96 kJ/mol (dashed yellow curve in Figure 1). It is more likely that the reaction proceeds to form $N(OH)_2$* by hydrogenating O_1 with an unpaired electron in the nitro group. We observed that this step is moderately exothermic (-50 kJ/mol) with an activation barrier of 58 kJ/mol. After the intermediate R-$N(OH)_2$* is formed, hydrogenolysis of the N-OH bond forms H_2O. The calculated true energy barrier of this step is 69 kJ/mol with an energy gain of 79 kJ/mol.

Considering that the formation of the first water molecule is highly exothermic, and it leaves the intermediate with unsaturated bonds on the surface, the following elementary steps are unlikely to be rate-limiting. Therefore, we only compare herein the energies of the first three hydrogenation steps. The reaction goes downhill step by step and that the apparent energy barrier is 49 kJ/mol.[52] It should be noted that the intrinsic activation barriers for the first three hydrogenation steps are comparable (49, 58, and 69 kJ/mol). We also considered the adsorption of H* on Au one at each hydrogenation step, with an energy cost of 10 kJ/mol (Figure S3).[53] The resulting potential energy surface is plotted in Figure S4, suggesting that H adsorption plays a minor role in the exothermicity nature of every elementary step. To further determine the rate-determining step, we conducted the maximum rate analyses[54] on the first three hydrogenation elementary steps under experimentally relevant temperature and pressure conditions with entropy contribution included (Methods in Supporting Information) as in our previous study.[55] Note that though the 3rd elementary step appears to have the highest intrinsic barrier, its rate is not the slowest due to the two exothermic steps before it. Instead, the maximum rate analyses (Table S4) demonstrate that the first hydrogenation step has the lowest maximum rate, suggesting that the first step is rate-limiting. In the following we investigate the role of occupation of the empty states in 4-NPh reduction with an emphasis on the first hydrogenation step.

3.3 Calculated potential energy surfaces at excited states.

We first explore the molecular frontier orbitals that may be occupied by the excited electrons.[56] Figure 2A shows the density of states (DOS) projected on Au, 4-NPh, the substituted nitro group, O_1, and O_2, respectively. The DOS of pristine Au and 4-NPh are plotted in Figure S5A, S5B. When 4-NPh adsorbs on the Au surface, the molecular orbitals become less pronounced than them in the gas phase.

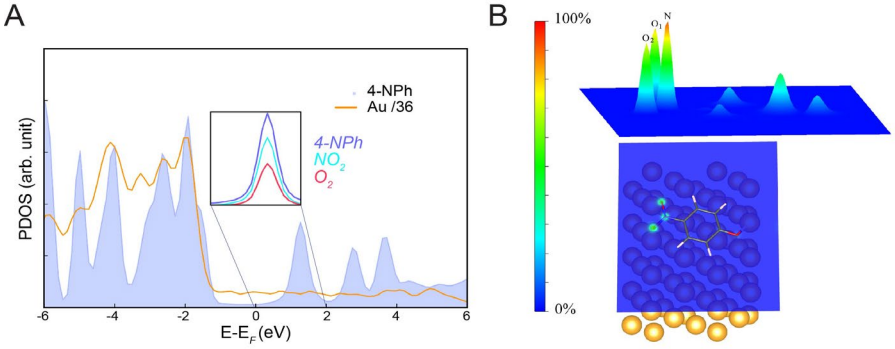

Figure 2. Electronic structure of 4-nitrophenol on Au (111) surface. A. The calculated density of states projected on the 4-NPh molecule, Au, NO_2 moiety and two oxygen atoms in the NO_2 moiety. The zero energy corresponds to the Fermi Energy (E_F). The inset shows the PDOS of the NO_2 moiety and two oxygen atoms compared with the PDOS of 4-NPh showing that the NO_2 group contributes largely to the frontier orbital of 4-NPh. The PDOS value of Au was reduced by 36 times to be comparable with the values of the other three parts. B. The spatial distribution of the molecular orbital that has the most charge contribution on the NO_2 moiety: top view (bottom) and side view (top).

The desired excitations are identified by analysis of calculated molecular orbitals, local densities of states, and charge densities. We calculated and analyzed each Kohn Sham (KS) orbital ranging from the E_F to 2.33 eV (LSPR peak) and identified a range of KS orbitals around 1.22 eV above the E_F that has significant charge distribution on the NO_2-moiety (Figure 2B). Since the LSPR peak of Au nanoparticles was found to locate at 532 nm (2.33 eV), if the reaction follows an indirect charge transfer mechanism, the collective electronic transition could lead to a wide distribution of hot electron from E_F to 2.33 eV.[10,57] In principle, this energy range is sufficient for excited electrons to access the antibonding states of 4-NPh. Figure S6 shows the change in charge densities between the resonance calculation (electronic excitation of 1.22 eV) and the ground-state

calculation when 4-NPh coadsorbs with H on the surface, indicating significant electron population on the NO_2 moiety at initial state.

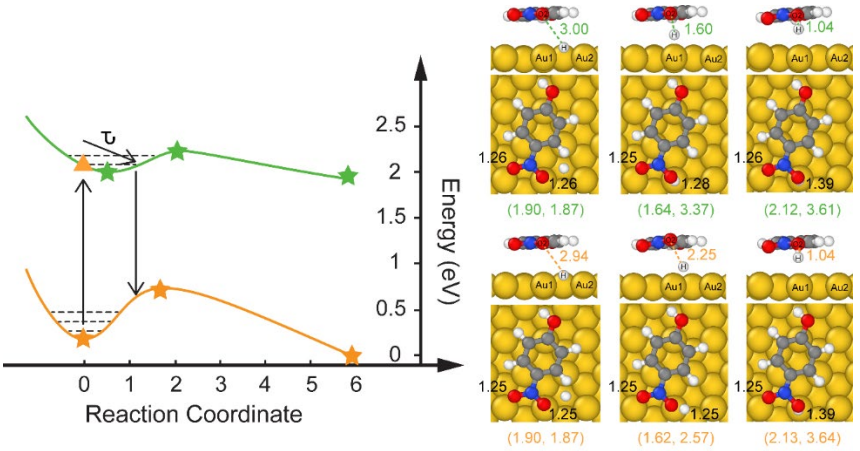

Figure 3. Reaction profile of the first hydrogenation step in the reduction of 4-NPh on Au(111) surface at the ground state (orange curve) and electron excitation of 1.22 eV (green curve). The values next to the molecule are bond lengths of N-O. The values in parentheses are $d_{Au1\text{-}H}$ and $d_{Au2\text{-}H}$, respectively. Stars represent the initial state, transition state, and final state of the rate-limiting step on the ground-state and excited-state potential energy surfaces. The corresponding structures are shown on the right panel. The vertical energy difference between orange triangle on the ground-state PES and star on the excited-state PES is the excitation energy.

We expect that, if electronic excitation to this electronic state can lower the energy barrier for the RDS, which would substantially promote the overall reaction, assuming that the barriers of the other elementary steps are not influenced significantly. Thus, we examined the potential energy surface for the kinetically relevant step – hydrogenation of the oxygen in the NO_2 moiety – with an electron added using the ΔSCF approach to simulate the reaction under green light irradiation.[44,58] Upon charging NO_2 moiety with one additional electron, the N-O1 and N-O2 bond lengths are slightly stretched from 1.25 to 1.26 Å. The electronic excitation of 1.22 eV results in an apparent displacement of the location of the ground state minimum (initial state) in the excited-state PES, as compared to the ground state. At transition state, it can be observed that O_2 in the NO_2 moiety of 4-NPh is a bit further away from the surface, and the N-O2 bond length is further stretched to 1.28 Å. Meanwhile, the O-H bond length at the transition state on the excited PES is much shorter than it at the ground state (2.25 Å vs 1.60 Å), showing a late transition state feature,

suggesting that the transition state is stabilized with this additional electron. The atomic displacement in Figure 3 may originate from the excited molecule having an extra electron in its antibonding orbital, thus changing in the equilibrium bond length of NO_2.

If the electron is added to the orbital at 1.22 eV above the E_F, the system could be excited up to 1.8 eV higher than the ground state. We estimated the vertical excitation energy of 1.8 eV following the equation below:

$$E_{excitation} = E_{ES} - E_{GS} \quad (4)$$

Where E_{GS} is obtained at ground state minimum, and E_{ES} is calculated self-consistently (with extra charge in the KS orbital but no relaxation), modeling the instantaneous restructuring of the electronic environment at the same atomic structure (a vertical excitation in Figure 3). This value of vertical excitation energy corresponds well, considering the approximately nature of our surface models, to the experimentally employed photon energy for nitrophenol hydrogenation at 2.33 eV. If the reactant travels on the excited PES (with sufficient lifetime), the activation barrier of the RDS could reduce from 0.50 to 0.21 eV. This result is in good agreement with our experimental observation discussed above that the catalytic activity of 4-NPh reduction to 4-APh on Au NPs is enhanced under light illumination. However, it is difficult to compare quantitatively our model and experimental results, because other factors not considered here in our model (e.g. solvent effects on the intermediates and transition states, mass transfer from liquid to the catalyst surface, and surface coverage effects) may influence the exact values of rates and activation barriers. On the other hand, given the fact that the resonance last on the time scale of femtoseconds, whereas the bond formation is on the picosecond scale, the resonance may decay before completing the bond formation. In this case, even if the electron decays before completing the RDS, the decay to the ground state PES can deposit the energy into the vibrational degree of freedom and optimally (consider one vibrate) reduce the energy barrier. The calculation indicates that the rate enhancements may be caused by charge transfer creating a transient negative ion (leaving the hole at the metal Fermi surface) to travel on the excited-state PES in the presence of light or dissipating the kinetic energy into the vibration of the chemical bonds to overcome a reduced activation barrier.

To determine if the reduction of the activation barrier is orbital selective, we considered other pronounced KS orbitals including the one right above E_F and a molecular orbital dominated by the aromatic ring. In both cases, similar amounts of reduction in the energy barrier were found (Table S1). To explain this insensitive orbital selectivity, the Bader charge analysis was performed.

When an extra electron was positioned into the aforementioned NO_2-dominate orbital, we expected to see approximately a unit charge population on the reactant; however, we found 0.7e in the metal, and only 0.3e on the 4-NPh (Figure S6, electron populates not only the 4-NPh molecule but also the Au surface). This charge delocalization was previously pointed out by Gacnholt et. al.[43] and thus is not surprising, because Au NPs have extended s orbitals, which overlaps with the adsorbate molecular frontier orbitals (Figure S7). At the occupied states in the DOS plot, there is strong hybridization between Au and the molecule, as a result of the dominant feature of Au d orbital and O p orbital in the energy range from -4 to -1 eV as referenced to the E_F. Although there is weak hybridization between Au and 4-NPh in the unoccupied states, the available s states of 64 Au atoms are still high with respect to the available states of 4-NPh. It is worth mentioning that this strong charge delocalization may imply possible direct charge transfer within the metal-molecule complex as discussed below.

3.4 Calculated reaction profile of the decoupled 4-nitrophenol.

To overcome the charge delocalization issue, which limits the charge that can be localized on the targeted molecular orbital, we propose here to cover the Au core with a thin layer of insulating material, e.g., hexagonal boron nitride (*h*-BN), and thus integrating a metal-free catalytic material with plasmonically-active light-absorbing antenna. Note growth of h-BN on Au substrates is feasible as demonstrated experimentally.[59,60] The *h*-BN nanosheets possess band gaps close to 6 eV, which are insensitive to the thickness.[61] To enhance the catalytic property of this chemically inert system, a carbon atom is employed as a dopant in the *h*-BN monolayer by replacing one of the N atoms with a C atom (CBN), which is a common type of defects in *h*-BN.[62] Introduction of the C is to anchor the hydrogen, which otherwise diffuses on the surface, to test the role of charge transfer in the same hydrogenation reaction.

At the ground state, 4-NPh prefers to adsorb on CBN at a parallel adsorption mode with two oxygen atoms being on top of the two corresponding boron atoms that are neighbors to the C atom (Figure 4B). The adsorption energy is -65 kJ/mol, which is weaker than that on Au. The O_1 is 3.25 Å from the surface B atom, and the distance between O_2 and the nearest B atom is 3.33 Å. As expected, H prefers to adsorb on the C dopant on the h-CBN surface with an adsorption energy of -177 kJ/mol, indicating a very strong chemisorption, mainly due to the unpaired electron in C.

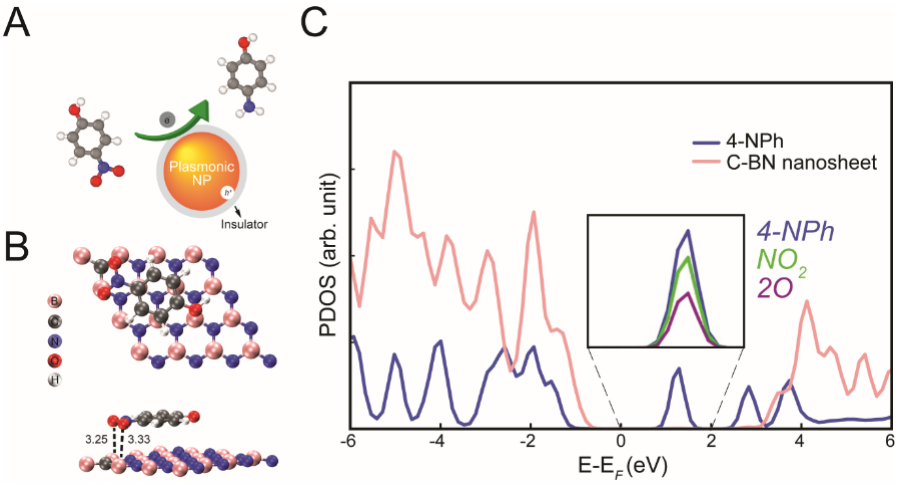

Figure 4. DFT-estimated geometric and electronic structure of 4-NPh on CBN(001) surface. A. Schematic of the proposed Au@CBN core shell structure. B. DFT-simulated adsorption structures of a 4-NPh molecule on the CBN. C. Projected density of states of 4-NPh molecule, CBN surface, the NO_2 moiety and two oxygen atoms in the NO_2 moiety. The zero energy corresponds to E_F. The inset shows the PDOS of the NO_2 and two oxygen atoms being compared with the PDOS of 4-NPh.

Next, we investigate the electronic structure of 4-NPh adsorbed on the CBN surface. As shown in Figure S8, the pure CBN surface shows a band gap of less than 4 eV, which is caused by the underestimation of the band gap in DFT calculations employing semi-local functionals.[63] Regardless, as expected, there is no overlap between CBN and 4-NPh states in the energy window ranging from E_F to 3 eV (Figure S9). In other words, by employing CBN as a substrate, the LUMO orbital of 4-NPh can be decoupled and easily distinguished. The weak hybridization between CBN and 4-NPh could in principle extend the lifetime of excited electrons by preventing the electron-hole recombination at the interface.[64] The decoupled LUMO is also confirmed by the fact that the LUMO level of pure 4-NPh has a similar shape in charge distribution compared to the LUMO of the adsorbed molecule (Figure S10). Note that Au was not included in the model shown in Figure 4 for simplicity; however, our model of the Au@CBN heterostructure (Figure S11) presents decoupled 4-NPh frontier orbitals, similar to 4-NPh adsorbed on the bare CBN surface (Figure S12). The feasibility of localizing charge on 4-NPh in the proposed Au@CBN heterostructure was tested and confirmed. The charge density difference between resonance calculation and ground state calculation on the CBN/Au(111) surface can be found in the supplementary information Figure S13.

We now compare the reaction profiles of the first hydrogenation step of 4-NPh reduction to 4-APh on the CBN surface. In Figure 5, we find that this step is barrierless at the ground state, equaling to the reaction energy of 1.87 eV. There is negligible charge transfer between the molecule and the substrate at the initial state (Table S2), indicating a character of physisorption. According to the PDOS plots, we identified an orbital with most wavefunction localized on the NO_2 group (~1.58 eV above E_F), which is exactly the orbital in the first peak above the E_F (Figure 4B). Figure S15 shows the change in charge density between the resonance calculation (electronic excitation of 1.58 eV) and the ground-state calculation for the molecules coadsorption with hydrogen on the CBN surface; the charge densities are pronouncedly localized at the 4-NPh molecule, as opposed to on the pure Au surface. As shown in Figure 5, when an electron is added in the first peak, the resultant reaction profile presents a significantly lower reaction energy (0.36 eV); the product R-NO(OH)* locates on top of the surface C, indicating that the reacting H travels a much shorter distance to the adsorbed 4-NPh (C-H bond length 3.08 Å at the ground state vs 1.63 Å at the excited state). Bader charge analysis on the initial state shows additional 0.89e on the molecule, and only 0.11e on the substrate, distinct from the previous case where most electrons are located on the Au substrate when no insulating material is inserted. Overall these calculations suggest that by inserting a thin layer of CBN, more charge could be localized on the molecule, which facilitates the formation of an O-H bond at the excited state as compared to the ground state.

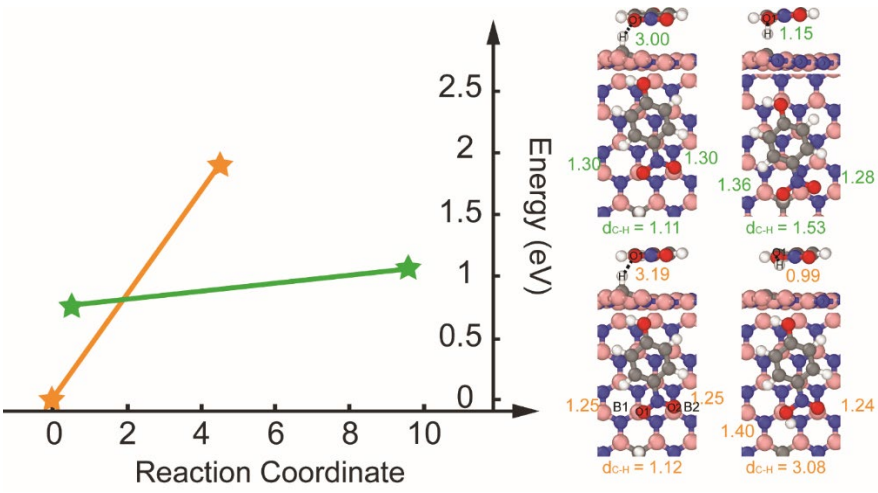

Figure 5. Reaction profile of the first hydrogenation step in the reduction of 4-NPh on CBN surface at the ground state (orange curve) and with an electron adding to the NO_2-driven orbital (green curve). The initial and final configurations at the ground state and the excited state are shown on the right.

Based on the discussion above, we propose a heterostructure that consists of a plasmonic metal and a thin insulating film for driving bond formation and dissociation, as illustrated in Figure 6. The E_F of the Au@CBN with adsorbed 4-NPh is set to zero. In this hybrid complex, the excited electrons may transfer indirectly by first being excited in the metal NPs upon photon absorption and thermalization, then tunneled through the thin layer of an insulator, and finally injected into the anti-bonding orbitals of the molecule (mechanism I in Figure 6). This hot carrier tunneling process was previously described in Halas and coworker's work on carrier generation in Al and tunnel of the hot carriers through a 2-4 nm self-limiting Al_2O_3 shell surrounding the Al core, followed by injection into the Cu_2O shell and the adsorbate.[57] Additionally, a recent study[22] suggested alternative LSPR relaxation channel through the CID mechanism (mechanism II in Figure 6). This direct charge transfer is challenging in the current system as it requires strong metal/adsorbate interaction,[7] while we found weak adsorption of 4-NPh on the Au/CBN surface (-63 kJ/mol). Furthermore, we consider that the interband transition in the CBN shell through resonance energy transfer may not be plausible because the vertical excitation energy (~4 eV) is beyond the range of visible light (~2.33 eV). Instead, the intramolecular electronic excitation within adsorbed 4-NPh is likely, following the non-radiative plasmon-induced resonance energy transfer, given the fact that the reduced HOMO-LUMO energy gap (~1.96 eV) in 4-NPh upon adsorption due to orbital renormalization, which is below the energy of photons from the 532 nm (2.33 eV) LED lamp (mechanism III in Figure 6). The hot electron mechanism (mechanism I in Figure 6) and the resonance energy transfer (mechanism III) are thus the most likely mechanism, compared to the CID across the interface and interband transition in the CBN. To unambiguously determine the mechanism, combined real-time TDDFT and ultrafast measurement of the interfacial charge dynamics will be valuable.

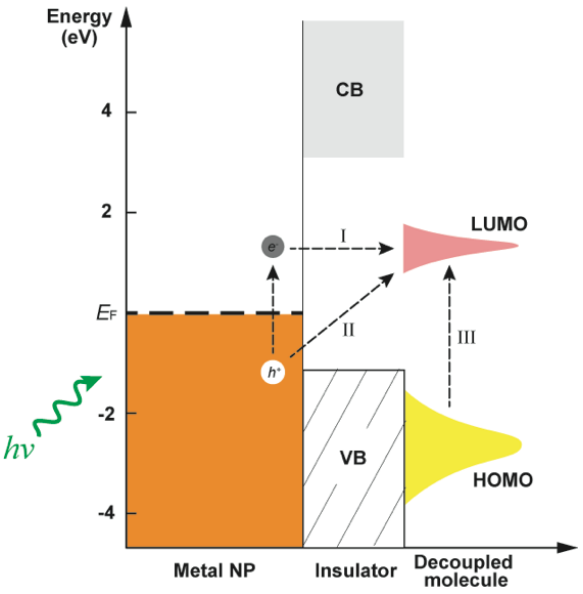

Figure 6. Energy band diagram of Au@CBN for plasmon-induced electron injection into the anti-bonding orbital of 4-NPh.

The nature of charge/energy transfer and injection process across the interface in the plasmonic systems remains unclear, as it is highly dependent on the studied system, and may involve synergistic LSPR effects including hot electrons, energy transfer, and localized electric field.[7] However, our study here provides an atomic picture of the charge transfer at interfaces, and suggest that the excited electrons need to occupy a targeted molecular orbital to enhance the kinetics of the rate-determining step. The insulator plays a key role by localizing electrons on the adsorbate to drive chemical reactions and increasing the lifetime of the excited states sufficiently to induce the bond dynamics.

4. Conclusions.

The LSPR-enhanced photocatalytic reduction reaction of 4-nitrophenol on a supported Au surface was investigated through a combination of experiments and computation. Specially, the catalytic activity on a supported Au catalyst with and without light irradiation was measured and a higher reaction rate under light irradiation was observed. This rate enhancement was correlated with the reaction energy profiles with and without electronic excitations from DFT calculations coupled with the delta SCF method. Our results suggest that population of electrons in the LUMO orbital elongate the N-O bond in nitrophenol and lowers the activation barrier of the rate-

determining step, leading to the enhanced rates in the experiments. However, caused by the hybridization of molecular frontier orbitals with the metal support, it is challenging to ambiguously identify the role of excited electrons in lowering the energy barrier. Thus, we propose and show that, by inserting a thin layer of carbon-doped BN, the Au@h-CBN core shell structure can localize excited electrons within the adsorbate, thus facilitating the hydrogenation step. We stress that the thin layer insulating material could adopt other candidates such as NaCl[65] and Cu_2N[66]. This work thus shed new insights into the optimization of plasmon-enhanced chemical reactions and may be valuable for the future design of plasmonic catalyst structure.

AUTHOR INFORMATION

Corresponding Author

*Email: wang_cbme@ou.edu

ORCID

Tong Mou: 0000-0003-1840-0515

Jhon Quiroz: 0000-0002-8626-7210

Pedro H. C. Camargo: 0000-0002-7815-7919

Bin Wang: 0000-0001-8246-1422

NOTES

There are no conflicts of interest to declare.

ACKNOWLEDGEMENTS

This work was financially supported by the Department of Energy (Grant No. DE-SC0020300). PHCC was supported by the Jane and Aatos Erkko Foundation, start-up funds from the University

of Helsinki, Academy of Finland, and the Helsinki Institute of Sustainability Science (HELSUS). The DFT calculations were performed using computational resources at the OU Supercomputing Center for Education & Research (OSCER) at the University of Oklahoma and the National Energy Research Scientific Computing Center (NERSC), a U.S. Department of Energy Office of Science User Facility. The authors acknowledge Dr. Jing Wen for his valuable discussions.

ASSOCIATED CONTENT

Supporting Information

The Supporting Information is available free of charge on the ACS Publication website.

4-NPh adsorption energetics and atomic structures on Au and CBN; potential energy profile for the 4-NPh hydrogenation with the adsorption of H included; projected density of states; figures showing charge accumulation with electronic excitation; a model structure for the CBN/Au(111) surface; spin density distribution; Bader charge analysis results; true activation barriers and imaginary frequencies for elementary steps in the main pathway; details on maximum rate analysis.

REFERENCES

(1) Zhang, Y.; He, S.; Guo, W.; Hu, Y.; Huang, J.; Mulcahy, J. R.; Wei, W. D. Surface-Plasmon-Driven Hot Electron Photochemistry. *Chem. Rev.* **2018**, *118* (6), 2927–2954. https://doi.org/10.1021/acs.chemrev.7b00430.

(2) Robatjazi, H.; Bao, J. L.; Zhang, M.; Zhou, L.; Christopher, P.; Carter, E. A.; Nordlander, P.; Halas, N. J. Plasmon-Driven Carbon–Fluorine (C(Sp3)–F) Bond Activation with Mechanistic Insights into Hot-Carrier-Mediated Pathways. *Nat. Catal.* **2020**, *3* (7), 564–573. https://doi.org/10.1038/s41929-020-0466-5.

(3) Martirez, J. M. P.; Carter, E. A. Prediction of a Low-Temperature N_2 Dissociation Catalyst Exploiting near-IR–to–Visible Light Nanoplasmonics. *Sci. Adv.* **2017**, *3* (12), eaao4710. https://doi.org/10.1126/sciadv.aao4710.

(4) Zhou, L.; Martirez, J. M. P.; Finzel, J.; Zhang, C.; Swearer, D. F.; Tian, S.; Robatjazi, H.; Lou, M.; Dong, L.; Henderson, L.; Christopher, P.; Carter, E. A.; Nordlander, P.; Halas, N. J. Light-Driven Methane Dry Reforming with Single Atomic Site Antenna-Reactor Plasmonic Photocatalysts. *Nat. Energy* **2020**, *5* (1), 61–70. https://doi.org/10.1038/s41560-019-0517-9.

(5) Brongersma, M. L.; Halas, N. J.; Nordlander, P. Plasmon-Induced Hot Carrier Science and Technology. *Nature Nanotech.* **2015**, *10* (1), 25–34. https://doi.org/10.1038/nnano.2014.311.

(6) Aslam, U.; Rao, V. G.; Chavez, S.; Linic, S. Catalytic Conversion of Solar to Chemical Energy on Plasmonic Metal Nanostructures. *Nat. Catal.* **2018**, *1* (9), 656–665. https://doi.org/10.1038/s41929-018-0138-x.

(7) Kale, M. J.; Avanesian, T.; Christopher, P. Direct Photocatalysis by Plasmonic Nanostructures. *ACS Catal.* **2014**, *4* (1), 116–128. https://doi.org/10.1021/cs400993w.

(8) Sytwu, K.; Vadai, M.; Hayee, F.; Angell, D. K.; Dai, A.; Dixon, J.; Dionne, J. A. Driving Energetically Unfavorable Dehydrogenation Dynamics with Plasmonics. *Science* **2021**, *371* (6526), 280–283. https://doi.org/10.1126/science.abd2847.

(9) Martirez, J. M. P.; Carter, E. A. Excited-State N2 Dissociation Pathway on Fe-Functionalized Au. *J. Am. Chem. Soc.* **2017**, *139* (12), 4390–4398. https://doi.org/10.1021/jacs.6b12301.

(10) Mukherjee, S.; Libisch, F.; Large, N.; Neumann, O.; Brown, L. V.; Cheng, J.; Lassiter, J. B.; Carter, E. A.; Nordlander, P.; Halas, N. J. Hot Electrons Do the Impossible: Plasmon-Induced Dissociation of H_2 on Au. *Nano Lett.* **2013**, *13* (1), 240–247. https://doi.org/10.1021/nl303940z.

(11) Mukherjee, S.; Zhou, L.; Goodman, A. M.; Large, N.; Ayala-Orozco, C.; Zhang, Y.; Nordlander, P.; Halas, N. J. Hot-Electron-Induced Dissociation of H2 on Gold Nanoparticles Supported on SiO2. *J. Am. Chem. Soc.* **2014**, *136* (1), 64–67. https://doi.org/10.1021/ja411017b.

(12) Zhou, L.; Swearer, D. F.; Zhang, C.; Robatjazi, H.; Zhao, H.; Henderson, L.; Dong, L.; Christopher, P.; Carter, E. A.; Nordlander, P.; Halas, N. J. Quantifying Hot Carrier and Thermal Contributions in Plasmonic Photocatalysis. *Science* **2018**, *362* (6410), 69–72. https://doi.org/10.1126/science.aat6967.

(13) Bao, J. L.; Carter, E. A. Surface-Plasmon-Induced Ammonia Decomposition on Copper: Excited-State Reaction Pathways Revealed by Embedded Correlated Wavefunction Theory. *ACS Nano* **2019**, *13* (9), 9944–9957. https://doi.org/10.1021/acsnano.9b05030.

(14) Cortés, E.; Xie, W.; Cambiasso, J.; Jermyn, A. S.; Sundararaman, R.; Narang, P.; Schlücker, S.; Maier, S. A. Plasmonic Hot Electron Transport Drives Nano-Localized Chemistry. *Nat. Commun.* **2017**, *8* (1), 14880. https://doi.org/10.1038/ncomms14880.
(15) Tong, F.; Liang, X.; Ma, F.; Bao, X.; Wang, Z.; Liu, Y.; Wang, P.; Cheng, H.; Dai, Y.; Huang, B.; Zheng, Z. Plasmon-Mediated Nitrobenzene Hydrogenation with Formate as the Hydrogen Donor Studied at a Single-Particle Level. *ACS Catal.* **2021**, *11* (7), 3801–3809. https://doi.org/10.1021/acscatal.1c00164.
(16) Quiroz, J.; Barbosa, E. C. M.; Araujo, T. P.; Fiorio, J. L.; Wang, Y.-C.; Zou, Y.-C.; Mou, T.; Alves, T. V.; de Oliveira, D. C.; Wang, B.; Haigh, S. J.; Rossi, L. M.; Camargo, P. H. C. Controlling Reaction Selectivity over Hybrid Plasmonic Nanocatalysts. *Nano Lett.* **2018**, *18* (11), 7289–7297. https://doi.org/10.1021/acs.nanolett.8b03499.
(17) Link, S.; El-Sayed, M. A. Spectral Properties and Relaxation Dynamics of Surface Plasmon Electronic Oscillations in Gold and Silver Nanodots and Nanorods. *J. Phys. Chem. B* **1999**, *103* (40), 8410–8426. https://doi.org/10.1021/jp9917648.
(18) El-Sayed, M. A. Some Interesting Properties of Metals Confined in Time and Nanometer Space of Different Shapes. *Acc. Chem. Res.* **2001**, *34* (4), 257–264. https://doi.org/10.1021/ar960016n.
(19) Christopher, P.; Xin, H.; Linic, S. Visible-Light-Enhanced Catalytic Oxidation Reactions on Plasmonic Silver Nanostructures. *Nature Chem.* **2011**, *3* (6), 467–472. https://doi.org/10.1038/nchem.1032.
(20) Spata, V. A.; Carter, E. A. Mechanistic Insights into Photocatalyzed Hydrogen Desorption from Palladium Surfaces Assisted by Localized Surface Plasmon Resonances. *ACS Nano* **2018**, *12* (4), 3512–3522. https://doi.org/10.1021/acsnano.8b00352.
(21) Kazuma, E.; Jung, J.; Ueba, H.; Trenary, M.; Kim, Y. Real-Space and Real-Time Observation of a Plasmon-Induced Chemical Reaction of a Single Molecule. *Science* **2018**, *360* (6388), 521–526. https://doi.org/10.1126/science.aao0872.
(22) Boerigter, C.; Campana, R.; Morabito, M.; Linic, S. Evidence and Implications of Direct Charge Excitation as the Dominant Mechanism in Plasmon-Mediated Photocatalysis. *Nat. Commun.* **2016**, *7* (1), 10545. https://doi.org/10.1038/ncomms10545.
(23) Rao, V. G.; Aslam, U.; Linic, S. Chemical Requirement for Extracting Energetic Charge Carriers from Plasmonic Metal Nanoparticles to Perform Electron-Transfer Reactions. *J. Am. Chem. Soc.* **2019**, *141* (1), 643–647. https://doi.org/10.1021/jacs.8b11949.
(24) Manjavacas, A.; Liu, J. G.; Kulkarni, V.; Nordlander, P. Plasmon-Induced Hot Carriers in Metallic Nanoparticles. *ACS Nano* **2014**, *8* (8), 7630–7638. https://doi.org/10.1021/nn502445f.
(25) Frischkorn, C.; Wolf, M. Femtochemistry at Metal Surfaces: Nonadiabatic Reaction Dynamics. *Chem. Rev.* **2006**, *106* (10), 4207–4233. https://doi.org/10.1021/cr050161r.
(26) Boerigter, C.; Aslam, U.; Linic, S. Mechanism of Charge Transfer from Plasmonic Nanostructures to Chemically Attached Materials. *ACS Nano* **2016**, *10* (6), 6108–6115. https://doi.org/10.1021/acsnano.6b01846.
(27) Lindstrom, C. D.; Zhu, X.-Y. Photoinduced Electron Transfer at Molecule−Metal Interfaces. *Chem. Rev.* **2006**, *106* (10), 4281–4300. https://doi.org/10.1021/cr0501689.
(28) Jia, C.; Li, X.; Xin, N.; Gong, Y.; Guan, J.; Meng, L.; Meng, S.; Guo, X. Interface-Engineered Plasmonics in Metal/Semiconductor Heterostructures. *Adv. Energy Mater.* **2016**, *6* (17), 1600431. https://doi.org/10.1002/aenm.201600431.

(29) Clavero, C. Plasmon-Induced Hot-Electron Generation at Nanoparticle/Metal-Oxide Interfaces for Photovoltaic and Photocatalytic Devices. *Nature Photon.* **2014**, *8* (2), 95–103. https://doi.org/10.1038/nphoton.2013.238.
(30) Kelly, K. L.; Coronado, E.; Zhao, L. L.; Schatz, G. C. The Optical Properties of Metal Nanoparticles: The Influence of Size, Shape, and Dielectric Environment. *J. Phys. Chem. B* **2003**, *107* (3), 668–677. https://doi.org/10.1021/jp026731y.
(31) Linic, S.; Christopher, P.; Ingram, D. B. Plasmonic-Metal Nanostructures for Efficient Conversion of Solar to Chemical Energy. *Nature Mater.* **2011**, *10* (12), 911–921. https://doi.org/10.1038/nmat3151.
(32) Kale, M. J.; Avanesian, T.; Xin, H.; Yan, J.; Christopher, P. Controlling Catalytic Selectivity on Metal Nanoparticles by Direct Photoexcitation of Adsorbate–Metal Bonds. *Nano Lett.* **2014**, *14* (9), 5405–5412. https://doi.org/10.1021/nl502571b.
(33) Jain, P. K.; Lee, K. S.; El-Sayed, I. H.; El-Sayed, M. A. Calculated Absorption and Scattering Properties of Gold Nanoparticles of Different Size, Shape, and Composition: Applications in Biological Imaging and Biomedicine. *J. Phys. Chem. B* **2006**, *110* (14), 7238–7248. https://doi.org/10.1021/jp057170o.
(34) Le, T.; Shao, Y.; Wang, B. Plasmon-Induced CO_2 Conversion on $Al@Cu_2O$: A DFT Study. *J. Phys. Chem. C* **2021**, *125* (11), 6108–6115. https://doi.org/10.1021/acs.jpcc.0c10957.
(35) Kresse, G.; Furthmuller, J. Efficient Iterative Schemes for Ab Initio Total-Energy Calculations Using a Plane-Wave Basis Set. *Phys. Rev. B* **1996**, *54* (16), 11169. https://doi.org/10.1103/PhysRevB.54.11169.
(36) Perdew, J. P.; Burke, K.; Ernzerhof, M. Generalized Gradient Approximation Made Simple. *Phys. Rev. Lett.* **1996**, *77* (18), 3865–3868. https://doi.org/10.1103/PhysRevLett.77.3865.
(37) Blochl, P. E. Projector Augmented-Wave Method. *Phys. Rev. B* **1994**, *50* (24), 17953–17979. https://doi.org/10.1103/PhysRevB.50.17953.
(38) Kresse, G.; Joubert, D. From Ultrasoft Pseudopotentials to the Projector Augmented-Wave Method. *Phys. Rev. B* **1999**, *59* (3), 1758–1775. https://doi.org/10.1103/PhysRevB.59.1758.
(39) Grimme, S.; Antony, J.; Ehrlich, S.; Krieg, H. A Consistent and Accurate Ab Initio Parametrization of Density Functional Dispersion Correction (DFT-D) for the 94 Elements H-Pu. *J. Chem. Phys.* **2010**, *132*, 154104. https://doi.org/10.1063/1.3382344.
(40) Henkelman, G.; Jónsson, H. A Dimer Method for Finding Saddle Points on High Dimensional Potential Surfaces Using Only First Derivatives. *J. Chem. Phys.* **1999**, *111* (15), 7010. https://doi.org/10.1063/1.480097.
(41) Henkelman, G.; Uberuaga, B. P.; Jónsson, H. A Climbing Image Nudged Elastic Band Method for Finding Saddle Points and Minimum Energy Paths. *J. Chem. Phys.* **2000**, *113* (22), 9901. https://doi.org/10.1063/1.1329672.
(42) Tang, W.; Sanville, E.; Henkelman, G. A Grid-Based Bader Analysis Algorithm without Lattice Bias. *J. Phys.: Condens. Matter* **2009**, *21* (8), 084204. https://doi.org/10.1088/0953-8984/21/8/084204.
(43) Gavnholt, J.; Olsen, T.; Engelund, M.; Schiøtz, J. Δ Self-Consistent Field Method to Obtain Potential Energy Surfaces of Excited Molecules on Surfaces. *Phys. Rev. B* **2008**, *78* (7), 075441. https://doi.org/10.1103/PhysRevB.78.075441.
(44) Hellman, A.; Razaznejad, B.; Lundqvist, B. I. Potential-Energy Surfaces for Excited States in Extended Systems. *J. Chem. Phys.* **2004**, *120* (10), 4593–4602. https://doi.org/10.1063/1.1645787.

(45) Barbosa, E. C. M.; Fiorio, J. L.; Mou, T.; Wang, B.; Rossi, L. M.; Camargo, P. H. C. Reaction Pathway Dependence in Plasmonic Catalysis: Hydrogenation as a Model Molecular Transformation. *Chem. Eur. J.* **2018**, *24* (47), 12330–12339. https://doi.org/10.1002/chem.201705749.

(46) Zhang, L.; Cao, X.-M.; Hu, P. Insight into Chemoselectivity of Nitroarene Hydrogenation: A DFT-D3 Study of Nitroarene Adsorption on Metal Surfaces under the Realistic Reaction Conditions. *Appl. Surf. Sci.* **2017**, *392*, 456–471. https://doi.org/10.1016/j.apsusc.2016.09.031.

(47) Millán, R.; Liu, L.; Boronat, M.; Corma, A. A New Molecular Pathway Allows the Chemoselective Reduction of Nitroaromatics on Non-Noble Metal Catalysts. *J. Catal.* **2018**, *364*, 19–30. https://doi.org/10.1016/j.jcat.2018.05.004.

(48) Liu, B. H.; Li, Z. P. A Review: Hydrogen Generation from Borohydride Hydrolysis Reaction. *J. Power Sources* **2009**, *187*, 527–534. https://doi.org/10.1016/j.jpowsour.2008.11.032.

(49) Guella, G.; Patton, B.; Miotello, A. Kinetic Features of the Platinum Catalyzed Hydrolysis of Sodium Borohydride from 11B NMR Measurements. *J. Phys. Chem. C* **2007**, *111* (50), 18744–18750. https://doi.org/10.1021/jp0759527.

(50) Wunder, S.; Polzer, F.; Lu, Y.; Mei, Y.; Ballauff, M. Kinetic Analysis of Catalytic Reduction of 4-Nitrophenol by Metallic Nanoparticles Immobilized in Spherical Polyelectrolyte Brushes. *J. Phys. Chem. C* **2020**, *114* (19), 8814–8820. https://doi.org/10.1021/jp101125j.

(51) Bae, S.; Gim, S.; Kim, H.; Hanna, K. Effect of NaBH4 on Properties of Nanoscale Zero-Valent Iron and Its Catalytic Activity for Reduction of p-Nitrophenol. *Appl. Catal. B* **2016**, *182*, 541–549. https://doi.org/10.1016/j.apcatb.2015.10.006.

(52) Kuroda, K.; Ishida, T.; Haruta, M. Reduction of 4-Nitrophenol to 4-Aminophenol over Au Nanoparticles Deposited on PMMA. *J. Mol. Catal. Chem.* **2009**, *298*, 7–11. https://doi.org/10.1016/j.molcata.2008.09.009.

(53) Lucci, F. R.; Darby, M. T.; Mattera, M. F. G.; Ivimey, C. J.; Therrien, A. J.; Michaelides, A.; Stamatakis, M.; Sykes, E. C. H. Controlling Hydrogen Activation, Spillover, and Desorption with Pd–Au Single-Atom Alloys. *J. Phys. Chem. Lett.* **2016**, *7* (3), 480–485. https://doi.org/10.1021/acs.jpclett.5b02400.

(54) Farberow, C. A.; Dumesic, J. A.; Mavrikakis, M. Density Functional Theory Calculations and Analysis of Reaction Pathways for Reduction of Nitric Oxide by Hydrogen on Pt(111). *ACS Catal.* **2014**, *4* (10), 3307–3319. https://doi.org/10.1021/cs500668k.

(55) Zhao, Z.; Bababrik, R.; Xue, W.; Li, Y.; Briggs, N. M.; Nguyen, D.-T.; Nguyen, U.; Crossley, S. P.; Wang, S.; Wang, B.; Resasco, D. E. Solvent-Mediated Charge Separation Drives Alternative Hydrogenation Path of Furanics in Liquid Water. *Nat. Catal.* **2019**, *2* (5), 431–436. https://doi.org/10.1038/s41929-019-0257-z.

(56) Tacey, S. A.; Szilvási, T.; Xu, L.; Schauer, J. J.; Mavrikakis, M. The Role of Iron-Oxide Aerosols and Sunlight in the Atmospheric Reduction of Hg(II) Species: A DFT+U Study. *Appl. Catal. B* **2018**, *234*, 347–356. https://doi.org/10.1016/j.apcatb.2018.04.049.

(57) Robatjazi, H.; Zhao, H.; Swearer, D. F.; Hogan, N. J.; Zhou, L.; Alabastri, A.; McClain, M. J.; Nordlander, P.; Halas, N. J. Plasmon-Induced Selective Carbon Dioxide Conversion on Earth-Abundant Aluminum-Cuprous Oxide Antenna-Reactor Nanoparticles. *Nat. Commun.* **2017**, *8*, 27. https://doi.org/10.1038/s41467-017-00055-z.

(58) Jones, R. O.; Gunnarsson, O. The Density Functional Formalism, Its Applications and Prospects. *Rev. Mod. Phys.* **1989**, *61* (3), 689–746. https://doi.org/10.1103/RevModPhys.61.689.
(59) Camilli, L.; Sutter, E.; Sutter, P. Growth of Two-Dimensional Materials on Non-Catalytic Substrates: H-BN/Au(111). *2D Mater.* **2014**, *1* (2), 025003. https://doi.org/10.1088/2053-1583/1/2/025003.
(60) Zhang, Z.; Ji, X.; Shi, J.; Zhou, X.; Zhang, S.; Hou, Y.; Qi, Y.; Fang, Q.; Ji, Q.; Zhang, Y.; Hong, M.; Yang, P.; Liu, X.; Zhang, Q.; Liao, L.; Jin, C.; Liu, Z.; Zhang, Y. Direct Chemical Vapor Deposition Growth and Band-Gap Characterization of MoS_2 / *h* -BN van Der Waals Heterostructures on Au Foils. *ACS Nano* **2017**, *11* (4), 4328–4336. https://doi.org/10.1021/acsnano.7b01537.
(61) Li, L. H.; Chen, Y. Atomically Thin Boron Nitride: Unique Properties and Applications. *Adv. Funct. Mater.* **2016**, *26* (16), 2594–2608. https://doi.org/10.1002/adfm.201504606.
(62) Sinthika, S.; Kumar, E. M.; Thapa, R. Doped H-BN Monolayer as Efficient Noble Metal-Free Catalysts for CO Oxidation: The Role of Dopant and Water in Activity and Catalytic de-Poisoning. *J. Mater. Chem. A* **2014**, *2* (32), 12812–12820. https://doi.org/10.1039/C4TA02434F.
(63) Topsakal, M.; Aktürk, E.; Ciraci, S. First-Principles Study of Two- and One-Dimensional Honeycomb Structures of Boron Nitride. *Phys. Rev. B* **2009**, *79* (11), 115442. https://doi.org/10.1103/PhysRevB.79.115442.
(64) Xie, W.; Schlücker, S. Hot Electron-Induced Reduction of Small Molecules on Photorecycling Metal Surfaces. *Nat. Commun.* **2015**, *6*, 7570. https://doi.org/10.1038/ncomms8570.
(65) Olsson, F. E.; Persson, M.; Repp, J.; Meyer, G. Scanning Tunneling Microscopy and Spectroscopy of NaCl Overlayers on the Stepped Cu(311) Surface: Experimental and Theoretical Study. *Phys. Rev. B* **2005**, *71*, 075419. https://doi.org/10.1103/PhysRevB.71.075419.
(66) Choi, T.; Ruggiero, C. D.; Gupta, J. A. Incommensurability and Atomic Structure of c (2 × 2) N / Cu (100) : A Scanning Tunneling Microscopy Study. *Phys. Rev. B* **2008**, *78* (3), 035430. https://doi.org/10.1103/PhysRevB.78.035430.

For Table of Contents Only